Origami-based tunable truss structures for non-volatile mechanical memory operation

Hiromi Yasuda[1], Tomohiro Tachi[2], Mia Lee[1], and Jinkyu Yang[1]

[1]*Department of Aeronautics & Astronautics,*

University of Washington, Seattle, WA 98195-2400, USA

[2]*Graduate School of Arts and Sciences,*

University of Tokyo, Tokyo 153-8902, Japan

arXiv:1702.05402v1 [cond-mat.mes-hall] 11 Dec 2016

Abstract

Origami has recently received significant interest from the scientific community as a building block for constructing metamaterials [1–9]. However, the primary focus has been placed on their kinematic applications, such as deployable space structures [10–12] and sandwich core materials [13], by leveraging the compactness and auxeticity of planar origami platforms. Here, we present volumetric origami cells – specifically triangulated cylindrical origami (TCO) [14–20] – with tunable stability and stiffness, and demonstrate their feasibility as non-volatile mechanical memory storage devices. We show that a pair of origami cells can develop a double-well potential to store bit information without the need of residual forces. What makes this origami-based approach more appealing is the realization of two-bit mechanical memory, in which two pairs of TCO cells are interconnected and one pair acts as a control for the other pair. Using TCO-based truss structures, we present an experimental demonstration of purely mechanical one- and two-bit memory storage mechanisms.

Mechanical memory operations can be highly useful not only to mimic electronic/optical memory devices, but also to manage the flow of mechanical energy for sound isolation, heat insulation, and energy harvesting purposes [21–25]. These mechanical devices can be highly useful in harsh environments, such as space and nuclear power plants, where extreme thermal, mechanical, and radiation conditions can hinder the operation of electronic devices. The robustness of mechanical systems, together with nanoelectromechanical technologies, has indicated the possibility and effectiveness of mechanical memory storage and computing devices [26, 27]. In previous studies, however, the operations of mechanical memory devices are mostly limited to an individual one-bit memory level (few attempts on multi-bit memories, e.g., [28]), and the possibility of cross-linked operations across the neighboring bits has not been fully explored.

Here, we study how we can realize a two-bit mechanical memory operation by using origami cells. These origami units can function in a modular way, and they can interact with each other to demonstrate hierarchical, multi-bit memory operations. For this purpose, tunability of unit cells plays an important role to enable the coupling and bit-flipping behavior between the adjacent cells. We show that origami-based structures provide an excellent platform to manipulate their tunable mechanical characteristics, such as stability and stiffness, in a controllable manner.

Origami has been a popular building block to construct mechanical metamaterials [1–9]. In particular, an overconstrained quadrangular mesh origami such as Miura-ori pattern [10] has been studied extensively because it offers a single degree of freedom (DOF) mechanism of folding without relying on the elasticity of materials. Such a structure is called rigid foldable origami, or rigid origami, in which the kinematics of folding governs the behavior of the whole structure. This can be beneficial for the control of deployable planar structures, such as solar panels and sails [11, 12].

In this paper, we feature volumetric origami as a building block of tunable metamaterials that can store information. In contrast to the rigid planar origami, volumetric origami generally inherits a highly nonlinear elastic behavior, at the sacrifice of small deformation of panels.

The coupled behavior of folding and elastic deformation can result in versatile kinematic and dynamic motions. We here investigate the mechanics of volumetric origami, specifically triangulated cylindrical origami (TCO), which can develop coupled dynamics of axial and rotational motions during folding (Fig. 1a). Despite its simplicity, we find a rich tunability in this structure to enable the design of monostable/bistable, zero-stiffness, and bifurcation structures from one-parameter family of the initial geometry. By assembling multiple origami modules with designed initial conditions, we demonstrate the feasibility of mechanical memory storage units with non-volatile, bit-flipping behavior.

The TCO consists of repeating triangular arrays, which are characterized by valley crease lines (length a) and mountain crease lines (length b) as shown in Fig 1b. Top and bottom surfaces of the TCO unit cell are n-sided polygons (e.g., $n = 5$ in Fig. 1) with side length c. Since the TCO is not a rigid foldable origami, folding/unfolding motions cause the warping of each facet, which may result in surface fatigue and damage under repeated usage. To overcome this issue while preserving the key characteristics of the TCO, we replace its surfaces with purely elastic truss members, which support tension/compression by using linear springs (Fig. 1c; See Supplementary Movie 1 for the comparison between the paper- and truss-based TCO models). If we assume that the top and bottom surfaces always share the same rotational axis during folding/unfolding, we can characterize the shape of the unit cell by defining its height (h), relative angle between the top and bottom polygons (θ), and radius of the circle circumscribing the polygon (R). Note that for the sake of mathematical simplicity, θ is defined as an angle between OB and the perpendicular bisector of A_aA_b as shown in the top view of Fig 1c. Letting h_0 and θ_0 be the initial height and relative angle respectively, we can express deformations of the structure by axial displacement $u = -(h - h_0)$ where compression is defined to be positive, and rotational angle $\varphi = \theta - \theta_0$.

In this truss model, two crease lines a and b are intersecting at a vertex of the polygon (e.g., B in Fig. 1c). For the fabrication of this truss model, we need to secure space for mechanical

joints. Thus, we modify the geometry of the TCO model, such that the two crease lines avoid intersecting (Fig. 1d). The difference between the original (Fig. 1c) and modified (Fig. 1d) models is characterized by the correction of the relative angle (θ_{cal} in Fig. 1d). By adopting this modified model, we fabricate, test, and analyze four different types of the TCO structures in various combinations of h_0 and θ_0. Figure 1e-h show the graphical illustration of these four original models (top row) and the digital images of their modified physical prototypes (bottom row): (h_0, θ_0) = (90 mm, 46°), (150 mm, 40°), (140 mm, 92°), and (119 mm, 0°). In these models, we use R = 90 mm and θ_{cal} = 9.7°. See Methods and Supplementary Information for more details on the experimental configuration.

To understand the folding behavior of the TCO-based structure, we calculate the total elastic energy (U) stored in the TCO cell as a function of u and φ (Methods and Supplementary Information). The insets of Fig. 2a-d show the surface maps of U for the four models, where dark colored region indicates the valley of the minimum energy level. This highlighted region forms a near-curve trajectory in this configuration space, indicating that the TCO-based structure exhibits a near mechanism of single DOF. Thus, simultaneously compressive and rotational motions of the TCO will follow this trajectory to satisfy the minimum potential energy principle (Methods). We can also identify the change of the normalized energy (U/kh_0^2 where k is the elastic constant of the linear truss element) under non-dimensionalized axial compression (u/h_0) by imposing $\partial U/\partial\varphi = 0$ (see Supplementary Information and Supplementary Movie 2 for this uni-axial test). Figure 2a-d shows the energy plots, where solid curves denote analytical results predicted by the minimum potential energy trajectory in the inset surface maps. The experimental measurements (dashed curves) corroborate these analytical results.

Comparing the four plots in Fig. 2a-d, we observe remarkably different trends: monostable, bistable, zero-stiffness, and bifurcation behaviors, respectively. If (h_0, θ_0) = (90 mm, 46°), the structure possesses only one minimum energy state at $u = 0$ (Fig. 2a). Therefore, the total energy increases monotonically as the TCO cell is compressed, implying a monostable prop-

erty. If (h_0, θ_0) = (150 mm, 40°), there exist two local minimum states along the energy valley as shown in Fig. 2b, indicating bistability. The TCO-based structure can also exhibit zero tangential stiffness, so called zero-stiffness mode, in which the application of axial compression does not create significant axial force or torque at the initial stage. Therefore, the total energy increases at an extremely low rate around u = 0 (Fig. 2c). The discrepancy between the analytical and experimental results attributes to the friction of the mechanical joints in the truss elements. Nonetheless, we observe much smaller stiffness in this model compared to the previous two cases (0.26% and 0.18% in terms of the linearized initial stiffness compared to those of the monostable and bistable cases, respectively; see the force-displacement curves in Supplementary Information). We analytically find that this zero-stiffness mode can be obtained when $\theta_0 = \pi/2$. Interestingly, this mode is independent of k and h_0 (mathematical proof in Supplementary Information). This zero-stiffness mode can be potentially useful for impact absorption applications of origami, while maintaining its reusable and tailorable feature.

Lastly, we observe that the TCO-based truss can experience bifurcation if $\theta_0 = 0$ (Fig. 2d). That is, in the initial stage of the folding, the TCO-based structure is axially compressed without rotation. However, if it reaches a bifurcation point, there are three branches: one unstable branch (continuing pure compression without rotation as indicated by arrow 1 in Fig. 2d) and two stable branches (starting to develop twisting motions in one or the other direction as pointed by arrow 2 in Fig. 2d). The two different trends in the uni-axial testing verify this bifurcation behavior (Fig. 2d; see Supplementary Information and Supplementary Movie 3 for the specially devised uni-axial compression setup). Overall, the results from these four prototypes manifest versatile dynamics of the TCO, which can be controlled simply by altering its initial geometry (i.e., h_0 and θ_0, more details in Supplementary Information).

Using this TCO-based truss structure as a unit cell, we further investigate the folding mechanism of multi-cell structures composed of serially stacked TCO cells. We start with a two-cell structure that consists of identical monostable TCO units with $(h_0, \theta_0) = (90 \text{ mm}, 46°)$. They

are linked together by sharing the interfacial polygon (Fig. 3a). Note that the chirality of the TCO cells is important in the multi-cell architectures. In this two-cell level, we arrange the cells in the opposite chirality, i.e., $(h_0, \theta_0) = (90 \text{ mm}, \pm 46^\circ)$, such that they collectively show an interesting coupling motion. To test the dynamics of the combined structure, we fix the right end of the stacked prototype to the wall and impose precompression $u_C = 45$ mm to the left end of the system (Fig 3a). Then, the total elastic energy of the system will differ depending on the rotational angles of the two unit cells, characterized by φ_1 and φ_2. Note that these angles are measured with respect to the initial positions of the left and central polygons, respectively. The inset of Fig. 3b shows the analytical values of U as a function of φ_1 and φ_2, where the highlighted zone represents the valley of the minimum potential energy. We find that the pair of TCO cells collectively possess two local minimum states: one with the right cell folded and the other with the left cell folded (see the graphical illustrations in the inset of Fig. 3b). The normalized elastic energy can be re-plotted as a function of φ_1 by imposing $\partial U/\partial \varphi_2 = 0$. Figure 3b evidently shows a symmetric double-well potential. This demonstrates that a pair of monostable TCO cells can successfully form a bistable system, requiring energy to overcome the potential barrier for the transition between the two stable states. Please note that this potential barrier can be manipulated by controlling precompression, i.e., tunable potential barrier. Let '1' be the state where the first unit cell is folded, and '0' be the state where the second unit cell is folded. Then we can use this system as a TCO-based mechanical memory device, which can store bit information ('1' or '0') by exploiting the double-well potential. One advantage of this mechanical memory is its non-volatility, implying that it can store bit information stably without the necessity of external residual force. To change the states from '0' to '1' or vice versa, we control only φ_1 so that the two-unit cell system can switch its state (see Supplementary Information and Supplementary Movie 4 for experimental verification).

Now we demonstrate a two-bit memory operation. We use two pairs of the TCO cells, i.e., four identical units of the TCO-based truss elements (h_0 = 90 mm) in the sequence of θ_0 =

[46°, – 46°, 46°, – 46°]. Similar to the previous setup for the single bit operation, we fix the rightmost polygon to the wall in both translational and rotational directions, while we let the other polygons rotate freely. We apply precompression of $u_C = 50$ mm and 47.5 mm to the first and second pairs respectively, such that the two pairs maintain the specified compressed states throughout the operation. Here, we intentionally introduce distinctive u_C values to break symmetry, thereby inducing controlled coupling behavior between the two bits. (further details to be explained later). We first analyze the total elastic energy of the system in relation to the deformed status of the two single-bit memory units. We represent the deformation of these two pairs by measuring the rotational angles φ_1 and φ_3, which represent the twisted angles of the first and third polygons respectively with respect to their uncompressed positions (Fig. 4a). The analytical results are shown in Fig. 4b, where we identify four minimum energy states representing '00', '01', '10', and '11'. Here the first and second numbers indicate the first bit (left pair denoted in blue color in the inset of Fig. 4b) and second bit (right pair in red color) bit, respectively. For example, '10' is the state where the first bit shows '1', and the second bit shows '0', following the definition of on and off status from the memory operation as illustrated in Fig. 3b.

The next step is to test the operation of the two-bit memory. Unlike operations of conventional memories (i.e., manipulation of each bit one by one), we demonstrate a unique operation of the two-bit memory by utilizing controlled coupling behavior between the two bits. In particular, this operation flips the second bit if the first bit is '1', which indicates that the first bit can control the state of the second bit. In this process, however, the second bit does not affect the state of the first bit, thus exhibiting a one-directional coupling mechanism. We demonstrate this operation by applying a pulse input to the first bit and measuring the response from the second bit. For this, we impose a trapezoid-shaped waveform on φ_1 to alternates the condition of the first bit between '1' and '0' (Supplementary Information). The key point here is to verify that the onset of the control pulse (i.e., '1') can flip the information stored in the second bit.

This process can be represented by the following two cases: '00' $\rightarrow$ '11' and '01' $\rightarrow$ '10'. The former corresponds to the conversion of the second bit from off to on (i.e, '0' to '1'), while the latter implies the opposite case that the second bit changes from on to off (i.e, '1' to '0') as the first bit is turned on.

We start with demonstrating the first case ('00' $\rightarrow$ '11'). Figure 4c illustrates the conceptual chart of the sequential operation of φ_1 and the consequential change of φ_3. The corresponding evolution of the TCO pairs' states is plotted in Fig. 4d, where the red curve denotes the experimental result of φ_1 and φ_3 measured by non-contact laser Doppler vibrometry (Supplementary Information). The system is initially positioned at '00', as denoted by the state at (i) in Figs. 4c-d. As we apply the pulse input to the first bit (i.e., $\varphi_1 = -62^\circ$ to 62°), the first bit changes its state from '0' to '1' in the beginning of the operation. See the transition of red curve from point (i) to point (ii) in Fig. 4d. This onset of the first bit eventually flips the second bit from '0' to '1' (i.e., $\varphi_3 = -31^\circ$ to 28°, see the state (iii) in Fig. 4d and Supplementary Movie 5). Thus, we verify the transition from the initial state '00' to the final state '11' without resorting to any direct excitations applied to the second bit.

Next, we move on to demonstrate the second case of the two-bit memory operation ('01' $\rightarrow$ '10'). Since the previous operation started from '00', we need to first perform input preparation to change the initial state from '00' to '01'. For this, we apply the pulse input directly to the second bit to convert it from '0' to '1'. This pulse input to the second bit does not affect the first bit, because φ_1 is not constrained. Therefore, φ_1 and φ_3 rotate in the same direction at the same rate without flipping the status of the first bit (see the input preparation process in Fig. 4e). Now we apply the pulse input to the first bit, which manipulates the first bit from '0' to '1' as shown by the trajectory of the red curve from the state (i) to the top right corner (ii). Sequentially, the energy state moves from the state (ii) to the state (iii), flipping the second bit from '1' to '0'. Since distinctive u_C values are applied to the first and second bits, the energy slope from '11' to '10' is less than that from '11' to '01'. Therefore, we observe that the state changes from '11'

to ‘10’ instead of ‘11’ to ‘01’. This serial process eventually changes the combined states of the first and second bits from ‘01’ to ‘10’, successfully verifying the second case of the two-bit memory operation (Supplementary Information and Supplementary Movie 6).

Although we showed the versatile nature and potential of the TCO elements hierarchically from a single-cell, double-cell, up to four-cell levels in one dimension, we envision that it can be further extended to multi-dimensions, e.g., honey-comb like 3D clusters. This will function as a layer of mechanical memory storage and computing structures, which can also provide multi-functional features, such as rugged protective layers. Likewise, while this study explored only serial connections of origami cells, they can be also connected in parallel or coaxially, to achieve various functionalities. Moreover, origami can be scaled to miniaturized dimensions. The versatile nature of the TCO together with nanoelectromechanical systems (NEMS) has great potential to develop robust NEMS actuators and sensing devices. Also, the intrinsic nature of the TCO cells that interweave axial and torsional motions can be further exploited for dynamic purposes. Conclusively, the volumetric origami cells can pave a new way for designing novel engineering systems for mechanical computing and other purposes relying on their rich constitutive mechanics in a single-cell level and strong cohesion in a multi-cell level.

Methods

Principle of minimum total potential energy approach. By using the geometry of the TCO-based unit cell, we calculate the length of crease lines a and b (see Fig 1(c)) as follows:

$$\begin{aligned} a &= \sqrt{(h_0-u)^2 + 4R'^2 \sin^2\left(\frac{\varphi}{2} + \frac{\theta_0}{2} - \frac{\pi}{2n} + \theta_{\text{cal}}\right)} \\ b &= \sqrt{(h_0-u)^2 + 4R'^2 \sin^2\left(\frac{\varphi}{2} + \frac{\theta_0}{2} + \frac{\pi}{2n} - \theta_{\text{cal}}\right)} \end{aligned} \tag{1}$$

where R' and θ_{cal} are a modified radius of the circle circumscribing the cross-section and a calibrated angle to compensate for the difference between original and physical prototype models

(Please see Supplementary Information for details). Then, the total elastic energy is calculated as $U = \frac{1}{2}nk(a-a_0)^2 + \frac{1}{2}nk(b-b_0)^2$ where a_0 and b_0 are initial length of a and b, and k is a spring constant of the truss members. Also, the work is obtained by $W = Fu + T\varphi$ where F and T are the external force and torque applied to the TCO cell, respectively. Based on these expressions, the total potential energy (Π) is

$$\Pi(u,\varphi) = U - W = \frac{1}{2}nK(a-a_0)^2 + \frac{1}{2}nK(b-b_0)^2 - Fu - T\varphi \tag{2}$$

By applying the principle of minimum total potential energy (i.e., $\partial\Pi/\partial u = 0$ and $\partial\Pi/\partial\varphi = 0$), we obtain the analytical expressions of the two-DOF folding/unfolding motion of the TCO-based structure (Supplementary Information).

Prototype fabrication and compression test. We use acrylic plates tailored by a laser cutter for the top and bottom polygons, and 3D printed parts made of polylactic acid for universal joints to attach truss elements to the polygons. Stainless steel shafts (diameter is 3.18 mm) and linear springs (k = 3.32 kN/m for monostable, bistable, zero-stiffness models; k = 1.08 kN/m for bifurcation model) are used to form truss elements that support tension/compression. To obtain the mechanical properties of the prototypes, we build a customized testing setup where the prototype is placed horizontally and its bottom surface is mounted on a fixed wall. The top surface is supported by a ball bearing and stainless steel shaft, so that it can translate and rotate with minimal friction (Supplementary Information and Supplemental Movies 2–6).

Acknowledgments

We thank Mike Clark at CoMotion at the University of Washington for technical support. We also thank Hansuek Lee at KAIST and Hyochul Kim at Samsung Advanced Institute of Technology in Korea for helpful discussions. We are grateful for the support from the ONR (N000141410388) and NSF (CAREER-1553202).

Author contributions

H.Y. and M.L. conducted the research and interpreted the results, and J.Y. and T.T. provided guidance throughout the research. H.Y., T.T., and J.Y. prepared the manuscript.

Additional information

The authors declare that they have no competing financial interests. Correspondence and requests for materials should be addressed to Jinkyu Yang (email: jkyang@aa.washington.edu).

---

[1] Hawkes, E. et al. Programmable matter by folding. *Proc. Natl. Acad. Sci. U. S. A.* **107**, 12441 (2010).

[2] Schenk, M. & Guest, S. D. Geometry of Miura-folded metamaterials. *Proc. Natl. Acad. Sci.* **110**, 3276–3281 (2013).

[3] Lv, C., Krishnaraju, D., Konjevod, G., Yu, H. & Jiang, H. Origami based mechanical metamaterials. *Sci. Rep.* **4**, 5979 (2014).

[4] Cheung K., Tachi T., Calisch S. & Miura K. Origami Interleaved Tube Cellular Materials *Smart Materials and Structures* 23 (2014)

[5] Yasuda, H. & Yang, J. Reentrant Origami-Based Metamaterials with Negative Poissons Ratio and Bistability. *Phys. Rev. Lett.* **114**, 185502 (2015).

[6] Waitukaitis, S., Menaut, R., Chen, B. G. & van Hecke, M. Origami Multistability: From Single Vertices to Metasheets. *Phys. Rev. Lett.* **114**, 055503 (2015).

[7] Silverberg, J. L. et al. Origami structures with a critical transition to bistability arising from hidden degrees of freedom. *Nat. Mater.* **14**, 389–393 (2015).

[8] Filipov, E. T., Tachi, T. & Paulino, G. H. Origami tubes assembled into stiff, yet reconfigurable structures and metamaterials. *Proc. Natl. Acad. Sci.* **112**, 12321–12326 (2015).

[9] Overvelde, J. T. B. et al. A three-dimensional actuated origami-inspired transformable metamaterial with multiple degrees of freedom. *Nat. Commun* **7**, 10929 (2016).

[10] Miura, K. *Method of packaging and deployment of large membranes in space* Report No.618 (Institute of Space and Astronautical Science, 1985).

[11] Tsuda, Y. et al. Flight Status of IKAROS Deep Space Solar Sail Demonstrator. *Acta Astronaut* **69**, 833–840 (2011).

[12] Zirbel, S. A. et al. Accommodating Thickness in Origami-Based Deployable Arrays. *J. Mech. Des.* **135** (2013).

[13] Schenk, M., Guest, S. D., & McShane, G. J. Novel Stacked Folded Cores for Blast-resistant Sandwich Beams. *Int. J. Solids Struct.* **51**, 4196–4214 (2014).

[14] Miura, K. Proposition of pseudo-cylindrical concave polyhedral shells. in *Proceedings of IASS Symposium on Folded Plates and Prismatic Structures* 141–163 (1970).

[15] Kresling, B. Plant Design: Mechanical Simulations of Growth Pat- terns and Bionics. *Biomimetics* **3**, 105–122 (1995).

[16] Zhao, X., Yabo H., & Hagiwara, I. Optimal design for crash characteristics of cylindrical thin-walled structure using origami engineering. *Transactions of The Japan Society of Mechanical Engineers Series A* **76**, 10–17 (2010).

[17] Jianguo, C., Xiaowei, D., Ya, Z., Jian, F., & Yongming, T. Bistable Behavior of the Cylindrical Origami Structure With Kresling Pattern. *J. Mech. Des.* **137**, 061406 (2015).

[18] Hunt, G. W. & Ario, I. Twist buckling and the foldable cylinder: an exercise in origami. *Int. J. Non. Linear. Mech.* **40**, 833–843 (2005).

[19] Guest, S. D. & Pellegrino, S. The folding of triangulated cylinders, Part I: Geometric considerations. *J. Appl. Mech.* **61**, 773–777 (1994).

[20] Ishida, S., Uchida, H., & Hagiwara I. Vibration isolators using nonlinear spring characteristics of origami-based foldable structures. *Trans. JSME (in Japanese)* **80**, DR0384 (2014)

[21] Li, N., Ren, J., Wang, L., Zhang, G., Hänggi, P., & Li, B. Phononics: Manipulating heat flow with electronic analogs and beyond. *Rev. Mod. Phys.* **84**, 1045–1066 (2012).

[22] Liang, B., Guo, X. S., Tu, J., Zhang, D. & Cheng, J. C. An acoustic rectifier. *Nat. Mater.* **9**, 989–992 (2010).

[23] Maldovan, M. Sound and heat revolutions in phononics. *Nature*, **503**, 209–217 (2013).

[24] Cummer, S. A. Selecting the direction of sound transmission. *Science* 343, 495–496 (2014).

[25] Fleury, R., Sounas, D. L., Sieck, C. F., Haberman, M. R., & Al, A. Sound Isolation and Giant Linear Nonreciprocity in a Compact Acoustic Circulator. *Science* **343**, 516–519 (2014).

[26] Pott, V., Kam, H., Nathanael, R., Jeon, J., Alon, E., & Liu, T. J. K. Mechanical computing redux: Relays for integrated circuit applications. *Proceedings of the IEEE* **98**, 2076–2094 (2010).

[27] Lee, T., Bhunia, S., & Mehregany, M. Electromechanical computing at 500°C with silicon carbide. *Science* **329**, 1316–1318 (2010).

[28] Guo, A., Fu, Y., Wang, C., Guan, L., Liu, J., Shi, Z., Gu, Z., Huang, R., & Zhang, X. Two-bit memory devices based on single-wall carbon nanotubes: demonstration and mechanism. *Nanotechnology* **18**, 125206 (2007).

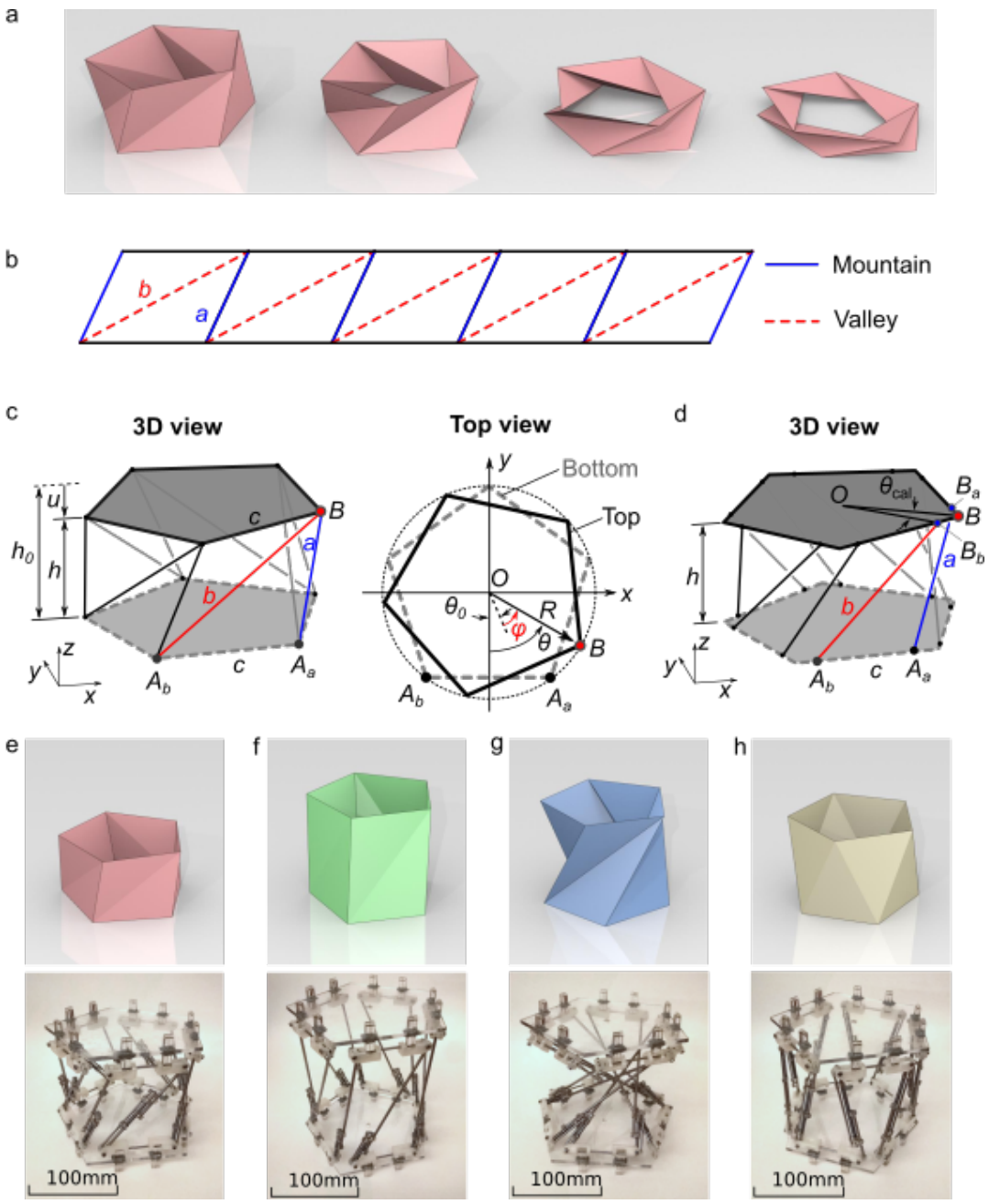

FIG. 1: **Geometry of triangulated cylindrical origami.** **a**, Folding motion of the TCO. **b**, The flat sheet with crease patterns consisting of mountain crease lines (a shown as blue solid lines) and valley crease lines (b shown as red dashed lines). **c**, Truss version of the TCO, where all facets are removed and crease lines are replaced by linear springs with a spring constant of k. **d**, Modified truss structure for the fabrication of physical prototypes. **e-h**, Graphical illustrations of four different TCO configurations (upper row) and digital images of their physical prototypes (lower row). Their initial configurations are (h_0, θ_0) = (90 mm, 46°), (150 mm, 40°), (140 mm, 92°), and (119 mm, 0°) from left to right.

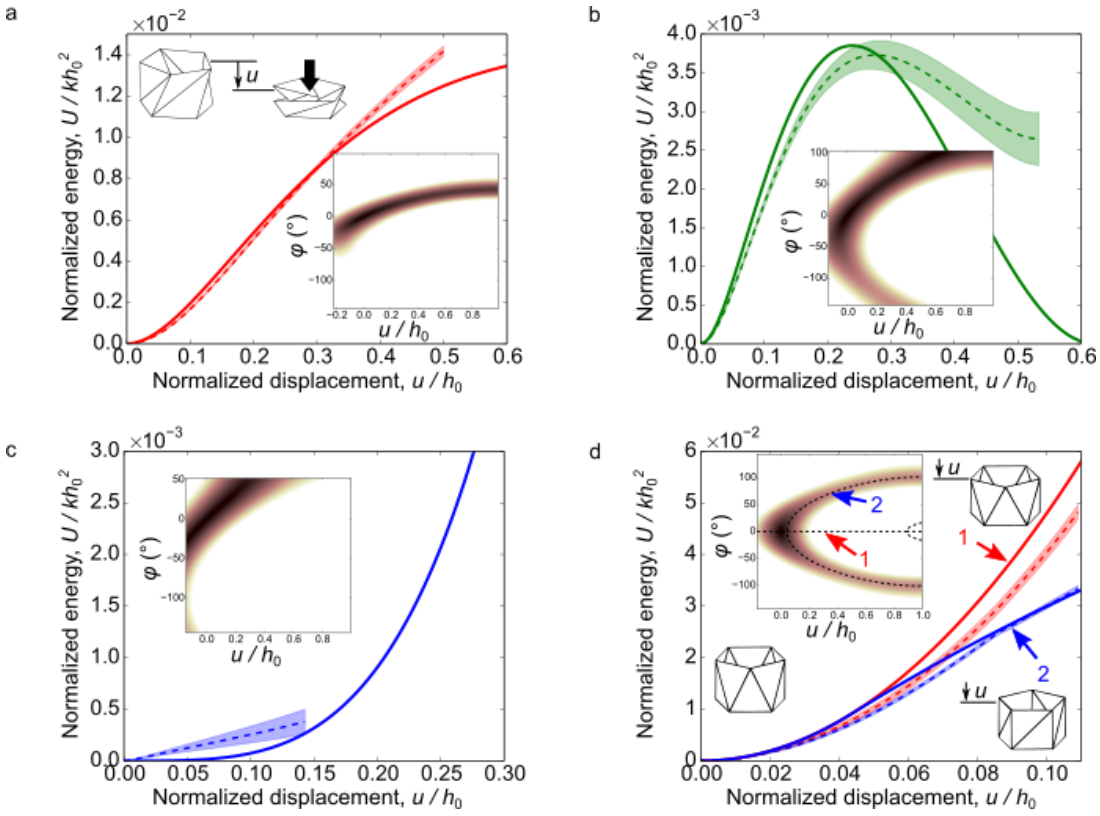

FIG. 2: **Folding motions of the TCO cells. (a-d)**, The energy analysis for the TCO-based truss structures shows remarkably different behaviors: **a**, Monostability at (h_0, θ_0) = (90 mm, 46°); **b**, bistability at (150 mm, 40°); **c**, zero-stiffness mode at (140 mm, 92°); and **d**, bifurcation at (119 mm, 0°). The displacement is normalized by h_0, and energy is normalized by kh_0^2. Experimental results (mean value is shown as dashed curves, and standard deviation is represented by colored areas) show qualitative agreements with the analytical predictions (solid curves). The inset plots show the equi-potential plots of U/kh_0^2 as a function of u/h_0 and φ, in which highlighted trajectories indicate the valley of minimum potential energy. In the experimental curves, the range of u/h_0 is restricted by the folding motions of the TCO-based truss prototypes. For example, the highly twisted shape of the zero-stiffness TCO prototype (Fig. 1g) causes the truss elements overlap in the early stage of folding, allowing only $\sim$15% of u/h_0 as shown in the panel **c**. The moderately twisted geometry of the monostable and bistable cases (Figs. 1e and f) permit more compression, allowing approximately 50% folding of the truss structure in terms of u/h_0 as shown in the panels **a** and **b**.

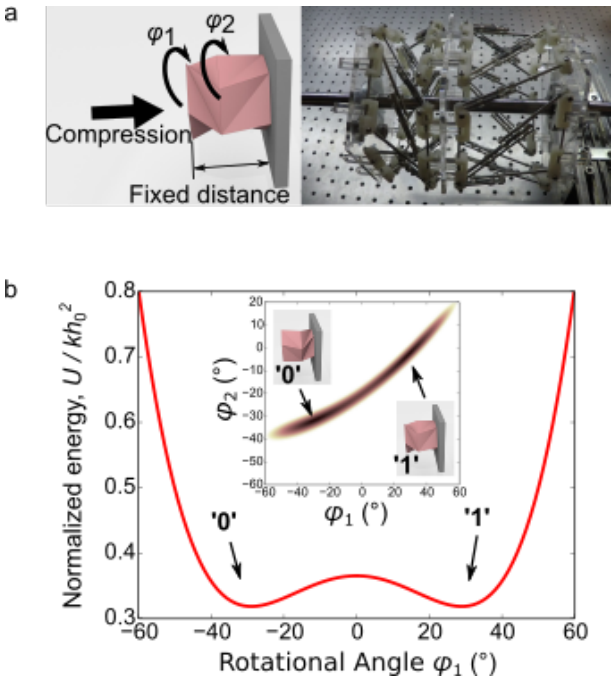

FIG. 3: **A pair of TCO cells' capability to demonstrate mechanical memory storage.** **a**, Two monostable TCO-based unit cells are connected horizontally. We fix the distance between leftmost and rightmost polygons by imposing a constant distance between them. Photograph of the corresponding configuration is shown in the right panel. **b**, The normalized elastic energy as a function of φ_1 shows the double-well potential numerically. The inset shows the surface map of the elastic energy as a function of both φ_1 and φ_2, where the highlighted region denotes the valley of the map corresponding to the minimum potential energy trajectory. There exist two minimum states, and the illustrations show the schematic shapes of the pair of TCO cells at these points. Here, the configuration of the folded right cell represents '0', while the one with the folded right cell denotes '1'.

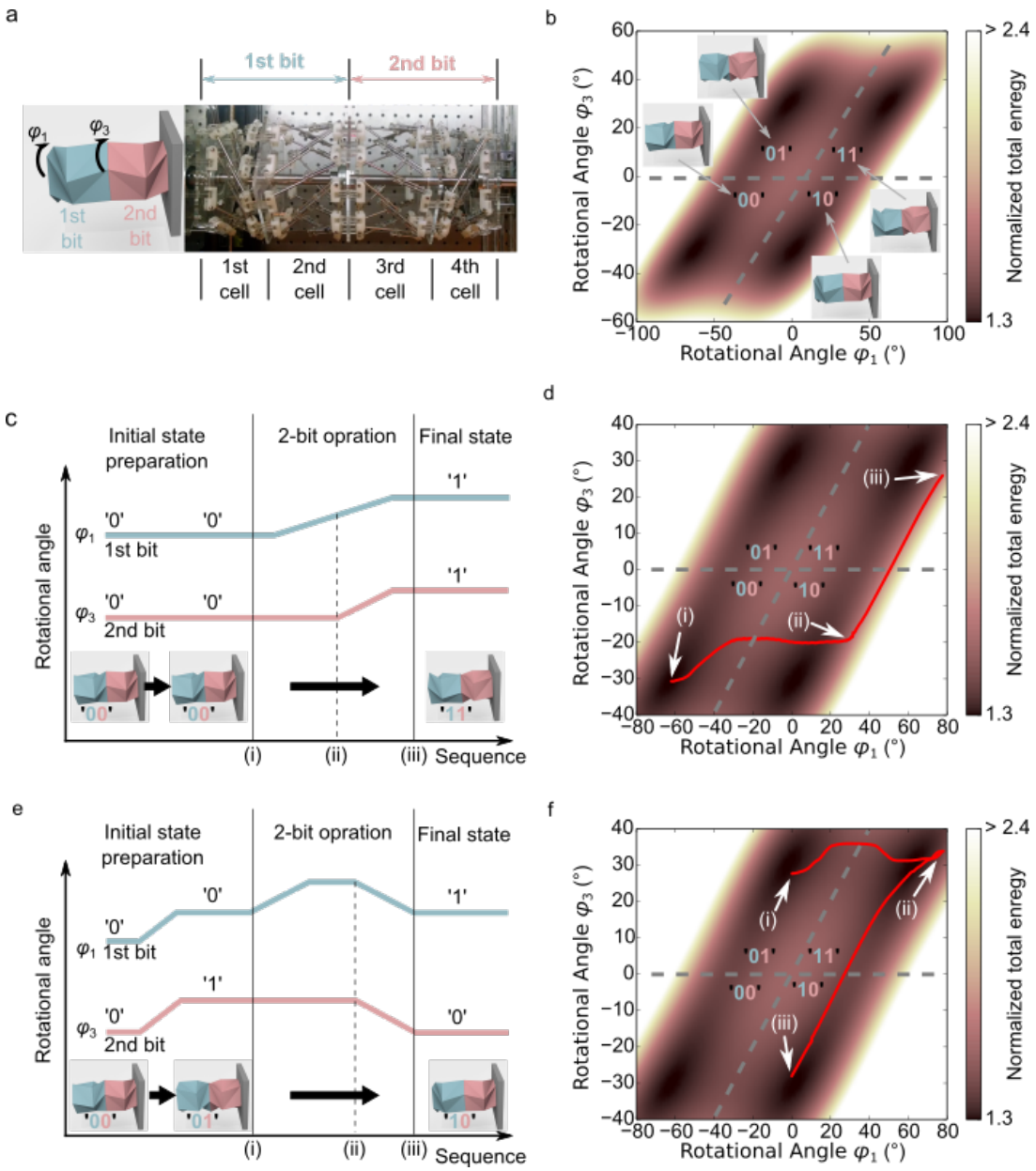

FIG. 4: **Two pairs of TCO cells' to demonstrate two-bit memory operation.** **a**, Two-bit memory is composed of four TCO-based unit cells as shown in a schematic illustration (left) and photograph (right). The first two units from the left (i.e., left pair in blue color) form a first bit, and the other two unit cells (i.e., right pair in red color) form a second bit. The states of these two bits are determined by the rotational angles of the first and third unit cells, φ_1 and φ_3. **b**, The potential energy of the system as a function of φ_1 and φ_3 is analyzed, where a darker region represents a lower level of the normalized potential energy (color map). We divide the φ_1 and φ_3 space into four regions: '00', '01', '10', and '11'. Inset illustrations indicate a representative shape of the TCO cells for each region. **c**, The sequence of the operation for '00' $\rightarrow$ '11' is shown. A pulse input is applied only to the first bit. **d** Experimental result in a red curve indicates that the operation flips the second bit from '0' to '1'. **e**, The sequence of the operation for '01' $\rightarrow$ '10' is shown. A pulse input is applied to the second bit first for the input preparation, and then to the first bit for the operation. **f** Experimental result indicates that the operation flips the second bit from '1' to '0'.